

1 Carbon, oxygen and biological productivity in the Southern Ocean

2 in and out the Kerguelen plume :CARIOCA drifter results.

3 L.Merlivat, J. Boutin, and F.d'Ovidio

4 Sorbonne Universités (UPMC, Univ Paris 06)-CNRS-IRD-MNHN, LOCEAN Laboratory, 4 place

5 Jussieu, F-75005 Paris, France

6

7 **Abstract**

8 *Keywords: Biological productivity regime: in situ measurements- Carbon-Oxygen*
9 *stoichiometry- Natural iron fertilization from the Kerguelen plateau- Iron control on carbon*
10 *biological production- Phytoplankton blooms extending downstream.*

11 The Kerguelen Plateau region in the Indian sector of the Southern Ocean supports annually a
12 large-scale phytoplankton bloom which is naturally fertilized with iron. As part of the second
13 Kerguelen Ocean and Plateau compared Study expedition (KEOPS2) in austral spring (Oct.-
14 Nov. 2011), one Carioca buoy was deployed east of the Kerguelen plateau. It drifted eastward
15 downstream in the Kerguelen plume. Hourly surface measurements of pCO₂, O₂ and ancillary
16 observations were collected between 1st November 2011 to 12 February 2012 with the aim of
17 characterizing the spatial and temporal variability of the biological Net Community
18 Production, NCP, downstream the Kerguelen plateau, assess the impact of iron-induced
19 productivity on the biological carbon consumption and consequently on the CO₂ flux
20 exchanged at the air-sea interface.

21 The trajectory of the buoy until mid December was within the longitude range, 72°E-83°E,
22 close to the polar front and then in the polar frontal zone, PFZ, until 97° E. From 17

23 November to 16 December, the buoy drifted within the Kerguelen plume following a filament
24 carrying dissolved iron, DFe, for a total distance of 700km.

25 In the first part of the trajectory of the buoy, within the iron plume, the ocean surface waters
26 are always a sink for CO₂ and a source for O₂, with fluxes of respective mean values equal to
27 -8 mmol CO₂ m⁻²d⁻¹ and +38 mmol O₂ m⁻²d⁻¹. Eastward, as the buoy escapes the iron enriched
28 filament, the fluxes are in opposite direction, with respective mean values of +5 mmol CO₂ m⁻²
29 d⁻¹ and -48 mmol O₂ m⁻²d⁻¹. These numbers clearly indicate the strong impact of biological
30 processes on the biogeochemistry in the surface waters within the Kerguelen plume in
31 November-mid December, while it is undetectable eastward in the PFZ from mid-December
32 to mid February.

33 While the buoy follows the Fe enriched filament, simultaneous observations of dissolved
34 inorganic carbon, DIC, and dissolved oxygen, O₂, highlight biological events lasting from 2 to
35 4 days. Stoichiometric ratios, O₂/C, between 1.1 and 1.4 are observed indicating new and
36 regenerated production regimes. NCP estimates range from 60 to 140 mmol C m⁻²d⁻¹. Based
37 on the relationship between the time a water parcel has left the plateau and its iron content, we
38 have highlighted that the main control on the value of NCP is the availability of iron in the
39 upper water column, with the largest NCP occurring in waters that have recently left the
40 plateau and presented the highest iron concentrations.

41 **1 Introduction**

42 The Southern Ocean is a key region for the global carbon cycle and the climate system. It
43 accounts for about 25–30% of the total anthropogenic carbon uptake. The Southern Ocean
44 (south of about 30°S) is found to be a sink area for atmospheric CO₂ in atmospheric or ocean
45 inversion models (Friedlingstein et al., 2006; Gruber et al., 2009) as well as in data based
46 approaches (Metzl et al., 1999; Takahashi et al., 2009). However, it represents a sink for
47 atmospheric CO₂ whose strength and future evolution are debated (Le Quere et al., 2010,
48 Lenton et al., 2013). Despite its importance, the Southern Ocean remains the region where
49 uncertainties regarding the air–sea CO₂ flux and the carbon budget are the highest (e.g.,
50 Gruber et al., 2009). This remote part of the global ocean is hardly accessible in winter,
51 leading to a very sparse spatiotemporal coverage of observations, including measurements of
52 surface pCO₂. Undersampling biases are aggravated by the high variability which
53 characterizes this oceanic region over a wide range of temporal and spatial scales.
54 Quantification of the impacts of thermodynamics, biology, and physics on the sea surface
55 partial pressure of CO₂, pCO₂, is a necessary step to understand the processes regulating the
56 ocean–atmosphere exchange of CO₂ and help to overcome the unresolved spatio temporal
57 variability effects.

58 The magnitude of the gradient of pCO₂ between the atmosphere and the surface ocean
59 depends on the relative contribution in the ocean mixed layer of the dynamic transport, the
60 thermodynamics and the biological activity. Biological net community production, NCP,
61 decreases sea surface pCO₂. In high nutrient-low-chlorophyll, HNLC, regions, including the
62 Southern Ocean, more than two decades of intense research have confirmed that increasing
63 iron supply stimulates primary production. (Boyd et al, 2007, Blain et al, 2008). Large and
64 persistent phytoplankton blooms develop annually in the vicinity of sub-Antarctic islands
65 (Blain et al., 2007; Borriane and Schlitzer, 2013; Pollard et al., 2009) due to natural iron

66 supply. The results of field studies in the vicinity of Crozet and Kerguelen islands have
67 clearly highlighted the crucial role of Fe on natural ecosystems and demonstrate the
68 stimulation of the biological carbon pump. In February 2005, the Kerguelen Ocean and
69 Plateau compared Study expedition, KEOPS1, focused on the high productivity area of the
70 Kerguelen Island during the peak and decline of the bloom (Blain et al, 2007). The results
71 emphasized the opportunity of studies on the Kerguelen plateau to investigate the functioning
72 of the biological carbon pump in a naturally iron-fertilized region. The KEOPS2 project in
73 October-November 2011, designed to improve the spatial and temporal coverage of the
74 Kerguelen region, was carried out in austral spring to document the early stages of the bloom
75 and to complement results of KEOPS1.

76 As part of KEOPS2 a CARIOCA buoy has been launched, drifted eastward close to the polar
77 front then entered the polar frontal zone, PFZ. NCP is deduced from high frequency pCO₂
78 measurements made in November-December along the trajectory of the drifter. The aim of the
79 present work is to provide a zoom on the extent of the iron seeding downstream the plateau
80 during the end of the spring, its effect on the production of organic carbon and its control of
81 the CO₂ air-sea flux

82

83 **2 Data and methods**

84 **2.1 Site description**

85 A Carioca buoy was deployed as part of the KEOPS2 expedition that took place from 9
86 October to 29 November 2011, in the Indian sector of the Southern Ocean in the vicinity of
87 the Kerguelen archipelago. It was deployed on 1st November 2011 over the Kerguelen plateau
88 and drifted eastward downstream within the Kerguelen plume. Until 12 February 2012, its
89 ~1800 kilometers long trajectory followed the polar front closely, entering the polar frontal
90 zone on the 16 December 2011 (figure 1). The buoy acquired data in the 72°E-75°E longitude

91 range of the intensive KEOPS 2 field campaign from 1st to 15 November 2011 and then was
92 advected downstream within the Kerguelen plume later in the season.

93 **2.2 Buoy measurements**

94 The Carioca buoy was equipped with a CO₂ sensor (Copin-Montegut et al., 2004; Hood and
95 Merlivat, 2001) and an Andraea F3835 optode to measure dissolved O₂ (Lefevre and
96 Merlivat, 2012). The partial pressure of CO₂, pCO₂, dissolved oxygen concentration, O₂, sea
97 surface temperature, SST, and sea surface salinity, SSS, were measured at a depth of 2 meters
98 on an hourly basis. Atmospheric pressure and wind speed are measured at a height of 2
99 meters, which were subsequently corrected to 10 meters height values. Collected data have
100 been transmitted by the buoy in real time via the Advanced Research and Global Observation
101 Satellite (Argos) data network.

102 Strictly, the CO₂ sensor measures the fugacity of CO₂, fCO₂, which is not identical to pCO₂
103 owing to the non-ideal nature of the CO₂ gas (Dickson et al, 2007). In the range of SST of our
104 study, the difference between pCO₂ and fCO₂ is close to 1.4 µatm, which is within the
105 instruments 3µatm absolute error. Accordingly, we will approximate fCO₂ as being equal to
106 pCO₂ within this study.

107 Alkalinity, Alk (µmol kg⁻¹), is computed from SST and sea surface salinity, SSS, using the
108 alkalinity-temperature-salinity relationship proposed by Lee et al. (2006) for the Southern
109 Ocean. Dissolved inorganic carbon, DIC (µmol kg⁻¹), is derived from pCO₂, Alk, SST and
110 SSS using the CO₂ dissociation constants of Mehrbach et al. (1973) as refitted by Dickson and
111 Millero (1987) and solubility from Weiss (1974). An accuracy of 10.5 µmol kg⁻¹ was
112 estimated, as a result of the combined uncertainties linked to the dissociation constants, the
113 accuracy of pCO₂ measurements and the uncertainty of the alkalinity derived from the
114 relationship proposed by Lee et al. 2006 (Boutin et al, 2008). The relative precision of

115 successive DIC values is expected to be $0.5\mu\text{mol kg}^{-1}$ (, Boutin et Merlivat, 2009, Merlivat et
116 al, 2014).

117 The oxygen optode measurements were calibrated initially in the laboratory prior to
118 deployment using a zero and 100% oxygen reference points. During the KEOPS 2 cruise, the
119 optode data were subsequently calibrated against the oxygen Winkler measurements made
120 with an accuracy of 0.2% (D.Lefèvre, personal communication) A constant offset of 13.6
121 $\mu\text{mol kg}^{-1}$ between the two techniques was found. Johnson [2010] compared the optode
122 measurements recorded at a time series off Monterey Bay, California, with shipboard
123 measurements made using the Winkler method. He found an offset between the two
124 techniques, which remained constant over the 5 months period of his record Therefore, we
125 simply apply an offset of $13.6\mu\text{mol kg}^{-1}$ to correct the optode data. Oxygen saturation, $O_{2\text{sat}}$
126 (in $\mu\text{mol kg}^{-1}$) is calculated using the equation of Garcia and Gordon (1992). The degree of O_2
127 saturation,(in percent), is given by:

$$128 \quad \% O_2 \text{ sat} = ([O_2] / [O_2^{\text{sat}}]) \times 100$$

129 **2.3 Calculation of air-sea fluxes of CO_2 and O_2**

130 The hourly air-sea CO_2 flux, F_{CO_2} ($\text{mmol m}^{-2} \text{d}^{-1}$), is derived from wind speed, the air-
131 sea gradient in pCO_2 and the gas transfer velocity [Boutin et al., 2008; Merlivat et al, 2014],
132 following:

$$133 \quad F_{CO_2} = k_{CO_2} \alpha_{CO_2} (pCO_{2\text{sea}} - pCO_{2\text{atm}}) \quad (1)$$

134 where α_{CO_2} is the solubility of CO_2 (Weiss, 1974), $pCO_{2\text{sea}}$ the partial pressure of CO_2 in
135 seawater (μatm), $pCO_{2\text{atm}}$ the partial pressure of CO_2 in the atmosphere (μatm), and k_{CO_2}
136 (cm/h) is the gas transfer velocity for CO_2 . $pCO_{2\text{atm}}$ is computed from the monthly molar
137 fraction xCO_2 at the Macquarie Island atmospheric station (NOAA/ESRL Global Monitoring

138 Division (<http://esrl.noaa.gov/gmd/ccgg/iadv>), the water vapor pressure of Weiss and Price
139 (1980) and the atmospheric pressure recorded on the drifter.

140 Injection of air bubbles below the air-water interface is neglected for the calculation of the
141 CO₂ flux but this contribution to the flux can be relatively important for oxygen. The equation
142 of the O₂ flux is then given by:

$$143 F_{O_2} = k_{O_2} ([O_2] - [O_{2sat}]) - F_{bub} \quad (2)$$

144 where k_{O_2} is the gas transfer velocity for O₂ and F_{bub} is the contribution of air bubbles using
145 the formula given by Woolf and Thorpe (1991):

$$146 F_{bub} = k_{O_2} 0.01(U/U_0)^2 [O_{2sat}] \quad (3)$$

147 with U the wind speed at 10m height in ms^{-1} and U_0 an empirically constant calibrated
148 specifically for O₂ of $9 ms^{-1}$. The total oxygen flux becomes:

$$149 F_{O_2} = k_{O_2} ([O_2] - [O_{2sat}]) (1 + 1.23 \cdot 10^{-4} U^2) \quad (4)$$

150 It results from this equation that the flux is positive when there is outgassing to the
151 atmosphere.

152 For both CO₂ and O₂, the gas transfer velocity is calculated using the formula of Sweeney
153 et al. (2007):

$$154 k = 0.27 U^2 (660/Sc)^{0.5} \quad (5)$$

155 where Sc is the Schmidt number, Sc_{CO_2} , for CO₂ or Sc_{O_2} for O₂ (Wanninkhof, 1992) and U
156 the 10m wind speed .

157 **2.4 Calculation of in-situ Carbon and Oxygen biological production**

158 Net community production, NCP_C , has been previously derived from drifting CARIOCA
159 buoys measurements, by looking at day-to-day evolution of DIC at dawn provided that daily
160 cycles of DIC in phase with the ones expected from biological activity are observed (Merlivat
161 et al, 2009, Boutin and Merlivat, 2009; Merlivat et al, 2014). In addition, in case O₂ is
162 measured, it is possible to simultaneously estimate NCP from O₂ day-to-day evolution,

163 NCP_{O₂} (Lefèvre and Merlivat, 2012). The method relies on hourly measurements of SST,
 164 SSS, pCO₂ and O₂ to estimate in-situ biological production from unattended platforms using a
 165 non-intrusive method. During the daylight period, photosynthesis, respiration, and air-sea
 166 exchange are mechanisms responsible for the change in DIC and O₂ recorded at 2m depth. If
 167 no significant change in salinity is observed, the processes of advection and mixing, and thus
 168 DIC and O₂ fluxes through the base of the mixed layer, h, are assumed to be negligible.
 169 Depending on atmospheric forcing, a warm diurnal layer, h*, can form during daylight
 170 (Merlivat et al., 2009). In this surface layer, of depth h*, from sunrise to sunset, due to
 171 combined effect of photosynthesis and respiration, DIC generally decreases and O₂ generally
 172 increases; they reach minimum, DIC_{min}, and maximum, O₂_{max}, values at the end of the
 173 day. At night, as a result of respiration and of the mixing between the warm layer and the
 174 mixed layer, DIC increases and O₂ decreases; they reach maximum, DIC_{max}, and minimum,
 175 O₂_{min}, values at the end of natural convection. NCP is derived from day-to-day change of
 176 DIC_{max} and O₂_{min}, after removing the contribution of the air-sea fluxes. Contribution of
 177 biological activity (photosynthesis plus respiration) during daylight is derived from DIC_{max}-
 178 DIC_{min}, and O₂_{min}-O₂_{max} after removing the contribution of the air-sea fluxes. Figure 2
 179 shows SST, DIC and O₂ over a 4 days period, 30 November-4 December 2011. The mean
 180 increase of SST equal to 0.044°C d⁻¹, superimposed on daily cycles of SST, indicates a
 181 stratification of the mixed layer over this 4 days period. No change of salinity is measured
 182 (not shown). Thus, the changes in DIC and O₂ observed during the 4 days were only driven
 183 by biological processes allowing the computation of NCP. The carbon and oxygen mass
 184 balance, either in the daytime interval during the development of the warm layer, h*, or over
 185 one day time interval in the mixed layer, h, result in the two following equations:

$$\left(\frac{\Delta \text{DIC}}{\Delta t} \right)_{\text{measured}} = \left(\frac{\Delta \text{DIC}}{\Delta t} \right)_{\text{bio}} + \left(\frac{\Delta \text{DIC}}{\Delta t} \right)_{\text{air-sea}} \quad (6)$$

187
$$\left(\frac{\Delta O_2}{\Delta t}\right)_{\text{measured}} = \left(\frac{\Delta O_2}{\Delta t}\right)_{\text{bio}} + \left(\frac{\Delta O_2}{\Delta t}\right)_{\text{air-sea}} \quad (7)$$

188 NCP integrated over the mixed layer is given by:

189
$$\text{NCP}_C = \rho h \frac{\Delta \text{DIC}_{\text{max}}}{\Delta t} + F_{\text{CO}_2} \quad (8)$$

190
$$\text{NCP}_{\text{O}_2} = \rho h \frac{\Delta O_{2\text{min}}}{\Delta t} + F_{\text{O}_2} \quad (9)$$

191 where F_{CO_2} and F_{O_2} are the air-sea CO_2 and O_2 flux ($\text{mmol m}^{-2} \text{d}^{-1}$), positive when there is
 192 outgassing to the atmosphere. h (- m) is the depth of the mixed layer, ρ (kg m^{-3}) is the density
 193 of seawater and $\Delta \text{DIC}_{\text{max}}/\Delta t$ and $\Delta O_{2\text{min}}/\Delta t$ ($\mu\text{mol.kg}^{-1} \text{d}^{-1}$) are the change of DIC (and O_2)
 194 between two consecutive maxima (and minima).

195 Between two consecutive mornings, at the end of nocturnal convection, $d\text{DIC}/dt_{\text{air-sea}}$ and
 196 $d\text{O}_2/dt_{\text{air-sea}}$ are equal respectively to F_{CO_2}/h and F_{O_2}/h , (where h is the mixed layer depth).
 197 During the daily stratification period, the diurnal mixed layer thickness decreases from h to h^*
 198 when DIC is minimum and O_2 is maximum. We make the assumption that it varies linearly
 199 from h to h^* in order to compute the hourly values of the air-sea flux contribution, $(F/h)_i$,
 200 which then are added over the daily stratification period. We assume that the minimum depth
 201 of the diurnal mixed layer, h^* , at the end of the production period is equal to the sampling
 202 depth 2m. A mixed layer depth equal to 20m has been adopted based on observations made
 203 during the KEOPS 2 field campaign under conditions similar to those encountered by the
 204 buoy. We will discuss later the uncertainties related to this choice.

205 **2.5 Chlorophyll and age distribution of the water parcels over and downstream of the**
 206 **Kerguelen plateau**

207 The time and spatial changes of the phytoplankton bloom as revealed by satellite ocean color

208 are shown in figure 3 (on which the buoy trajectory is indicated). The strongest bloom is
209 observed from 11 November to 2 December, about two months after bloom initiation,
210 followed by a clear decay early summer in December.

211 The horizontal transport of water parcels eastward of the Kerguelen plateau has been derived
212 from altimetry (d'Ovidio et al 2015). From this analysis, the time since a water parcel has left
213 the plateau (so called age of the water parcel) could be estimated. The trajectory of the
214 Carioca buoy was placed in this temporal framework using the age map of 25th November
215 (figure 4). Over the period 1st November to 31 December, the buoy has sampled a large range
216 of water parcels with different ages as shown by the stirring pathways east of the Kerguelen
217 plateau close to the trajectory of the drifter. NCP estimates have been made over the period 18
218 November-13 December (Tables 1 and 2).

219

220 **3 Results**

221 **3.1 Buoy measurements**

222 The variations of SST and SSS observed along the trajectory of the buoy are largely explained
223 by its position relative to the polar front, PF (figure 1). From 1st to 12 November, the buoy
224 was drifting in the meander of the PF (Park et al, 2014) with SST~3°C and SSS ~33.83. From
225 12 November to 16 December, while the buoy followed closely and sometimes crossed the
226 PF, SST is ~4.2°C and SSS ~33.75. During this time interval, simultaneous short time peaks
227 of SST (negative) and SSS (positive) were observed whilst transiting the PF (figures 1 and
228 5a). From 16 December 2011 to 11 February 2012, the buoy drifted in the polar frontal zone,
229 where higher temperature (close to 6°C) and higher salinity, (in the range 33.8 to 33.9) were
230 measured.

231 A very large variability of pCO₂ values, from ~280 μatm to ~400 μatm, are observed while
232 the buoy is drifting in the meander of the PF (figure 5c). Shipboard measurements of pCO₂
233 made during the KEOPS 2 field campaign show a similar range of variability (Lo Monaco et
234 al, 2014). During periods when the buoy is southward or close to the PF, the surface waters
235 are undersaturated in CO₂ relative to atmospheric CO₂. After 17 December, in the polar
236 frontal zone, the surface waters become supersaturated. Moreover, the surface waters are
237 supersaturated in oxygen until 16 December, with saturation values up to 110% (figure 5d). In
238 the polar frontal zone, data showed O₂ undersaturation

239 **3.2 Air-sea flux of CO₂ and O₂**

240 From 1st November to 17 December surface waters are a source of O₂ (figure 6a) for the
241 atmosphere and a sink of CO₂ (figure 6b). Conversely, in the polar frontal zone, east of 83°E,
242 we observe an ingassing of O₂ and outgassing of CO₂. It is worth noting that the absolute
243 values of the fluxes are larger for O₂ than for CO₂ due to the buffer factor of ocean water
244 carbonate chemistry. From 1st November to 16 December, the flux of O₂ and CO₂ are
245 respectively $38 \pm 34 \text{ mmol m}^{-2} \text{d}^{-1}$ and $-8.3 \pm 7.5 \text{ mmol m}^{-2} \text{d}^{-1}$. After 16 December, they are equal
246 respectively to $-48 \pm 43 \text{ mmol m}^{-2} \text{d}^{-1}$ and $5.3 \pm 4.7 \text{ mmol m}^{-2} \text{d}^{-1}$.

247 **3.3 Dissolved inorganic Carbon, DIC, and oxygen**

248 A significant reduction in DIC of $\sim 50 \mu\text{mol kg}^{-1}$ is observed from November 1st to December
249 17th, followed by an increase of approximately $20 \mu\text{mol kg}^{-1}$ when the buoy crossed the PF and
250 starts drifting northward in the polar frontal zone. At the same time, a sharp decrease of the
251 O₂ concentration is measured (figure 7). During the first part of the trajectory of the buoy
252 close and along the PF, the highly variable distribution of the concentrations of DIC and O₂
253 are controlled by physical transport processes, lateral advection and vertical mixing, air-sea
254 exchange, and biological processes. Four periods for DIC and O₂ of 3 to 5 days have been

255 identified when only air-sea exchange and biological processes control the change with time
256 of the concentrations of DIC and O₂, as described by equations 6 and 7 (cf. also figure 2). For
257 7 days during these periods, the amplitude of the difference between the extrema ($|\text{Max}-\text{min}|$)
258 for DIC and O₂ in the warm daily surface layer, h*, have been measured (table 1 and figure
259 8).

260 **3.4 Quantification of biological processes**

261 Large amplitudes of the diurnal cycles of DIC and O₂ up to 12 μmol kg⁻¹ have been measured,
262 while day-to-day changes peak at 5 μmol kg⁻¹ (figure 8). These numbers represent the
263 contribution of the biological processes plus the air-sea exchange terms (equations 6 and 7).
264 Their ratio is close to one (figure 8). In table 1, it is interesting to note the wide range of
265 values of CO₂ and O₂ air-sea fluxes, the O₂ fluxes being up to 6.6 larger than the CO₂ ones.
266 A summary of the biological and air-sea flux terms for DIC and O₂ is given in table 2. Figure
267 9 shows the simultaneous biological changes of O₂ and DIC observed in the ten selected
268 situations. The DIC measurements are used to calculate carbon NCP (equation 9 and table 2).
269 In November, 2 values of NCP respectively equal to 140±7 and 124±23 mmol C m⁻²d⁻¹ are
270 computed. In December, we have NCP equal to 60±12 and 72±17 mmol C m⁻²d⁻¹. The
271 standard deviation does not include the uncertainty on the choice of the value of the MLD.

272

273 **4 Discussion**

274 **4.1 Hydrodynamical environment along the trajectory of the buoy**

275 During the 2011 KEOPS2 cruise, Park et al (2014) determine and validate an up-to-date location
276 of the PF around the Kerguelen Islands over the longitude range, 68°E-78°E. The PF, defined as
277 the northern limit of the subsurface minimum of temperature, T_{min} of 2°C, was validated based on

278 in-situ hydrographic and current measurements made during the cruise, satellite ocean color
279 images, and altimetry-derived surface velocity fields. The PF location rounds the Kerguelen
280 Islands from the south, executing a permanent cyclonic meandering in the off-plateau area
281 immediately east of the Kerguelen Islands until the longitude of 73.5°E , then extends eastward
282 (figure 5, Park et al, 2014).

283 The buoy, after drifting inside the meander, traverses the front many times during which rapid
284 increases of salinity are observed (figures 1 and 5). Eastward of 78°E , the comparison of the two
285 routes cannot be so specific as the trajectory of the buoy is compared with a large scale
286 climatological PF (Park et al, 2009, 2011) which certainly doesn't take into account the highly
287 time-varying frontal circulation of the area. On 16 December, the latitude of the polar front as
288 derived from the buoy measurements (figures 1 and 5) is very close to the climatological PF.

289 **4.2 Lagrangian distribution of chlorophyll along the trajectory of the buoy**

290 The sequence of ocean color images on which is superposed the trajectory of the buoy from 11
291 November to 28 December (figure 3) show the rapid development of the bloom until 2 December and
292 then its decline. In most cases, the buoy follows the highly time-varying mesoscale meanders
293 observed within satellite chlorophyll images. In their detailed study of the location of the PF during
294 the KEOPS 2 cruise, Park et al (2014) put forward that the high-resolution chlorophyll concentration
295 images appear as an excellent marker of the fronts and filaments, supporting evidence for the
296 frontal circulation determined from the combined hydrography, altimetry, and drifters tracking
297 data. We then are led to conclude that the biological processes identified during 4 periods along
298 the trajectory of the buoy (figure 1 and table 1) are representative of frontal conditions which
299 favor biological production. Specifically, the data computed between 18 to 28 November, in the
300 longitude domain 76°E - 78°E , seem very tightly linked to the complex structures of the PF (figure
301 1).

302 **4.3 Carbon and oxygen biological production regimes**

303 During the KEOPS 2 expedition, MLD were estimated at 3 stations (TEW-7, TEW-8, F-L)

304 very close to the PF (Park et al, 2014), (figure 1). The average MLD at these stations,
305 calculated with the criteria: depth where the potential density = potential density at 10 m +
306 0.02 kg m^{-3} , was equal to 20 m (Park et al., 2014, Trull et al, 2015). We elect to use this depth
307 as our MLD definition, as physical (T, S) characteristics at these stations are very similar to
308 CARIOCA measurements (figure 5b). Furthermore, the choice of a relatively shallow mixed
309 layer, 20 meters, is supported by the work of Taylor and Ferrari (2012) who found, based on
310 numerical simulations, that restratification at fronts can inhibit vertical mixing, triggering
311 high latitude phytoplankton blooms. However, the values of NCP integrated over the depth of
312 the mixed layer may be an underestimate if the depth of the euphotic layer, Z_e , is greater than
313 MLD. During the KEOPS 2 expedition at the station F-L, Cavagna et al (2014), indicate
314 $Z_e=30$ meters. From the vertical profile of net primary production, NPP, based on the analysis
315 of carbon 13 incubation experiments, the computed value of NPP integrated over 20 meters
316 represents about 75% of NPP integrated over Z_e . NPP at depth greater than Z_e is negligible
317 close to 2%. We take into account an underestimation of 33% to compute NCP, as the
318 euphotic layer depth is larger than the MLD which is equal to 20 meters.

319 The values of the carbon net community production, which corresponds to DIC transformed
320 into particulate organic carbon, POC and dissolved organic carbon, DOC by biological
321 activity, vary from $130 \text{ mmolm}^{-2}\text{d}^{-1}$ between 23 and 28 November and then decreases to about
322 $65 \text{ mmolm}^{-2}\text{d}^{-1}$ at the beginning of December (table 2). A similar range of values of carbon net
323 community production along fronts in the Southern ocean have previously been observed
324 (Merlivat et al, 2014). During the KEOPS 1 expedition in 2005, Lefevre et al (2008) and
325 Jouandet et al (2008) measured NCP at 2 stations south of the polar front. At the same
326 locations, NCP measured at a five days interval varies between 105 and $43 \text{ mmol C m}^{-2} \text{ d}^{-1}$.
327 This illustrates the large spatial and temporal variability of processes which control NCP,
328 depending on the bathymetry and the physical and dynamical regime prevailing in the upper

329 layers in the KEOPS 2 field study

330 The biological terms, $\left(\frac{\Delta O_2}{\Delta t}\right)_{\text{bio}}$ and $-\left(\frac{\Delta \text{DIC}}{\Delta t}\right)_{\text{bio}}$ are represented on figure 9 on which the 2

331 lines with slopes equal to 1.4 and 1.1 indicate the expected oxygen-carbon relationship
332 respectively for a new production regime (photosynthetic quotient, PQ=1.4) or a regenerated
333 one, PQ= 1.1, (Laws, 1991), During daytime, DIC and O₂ variations represent GCP-R/2
334 (GCP, Gross Community Production, R, Respiration) if we assume the respiration rate
335 constant over a day. From dawn to dawn, it corresponds to GCP-R. As a result, the daytime
336 and the dawn to dawn ratio should be different, the difference being smaller when R is small
337 compare to GCP (autotrophy, high f ratio). On figure 9 within the errors bars, we can't
338 estimate the difference. Nevertheless, it appears that both regimes may have prevailed at
339 different times. This supports the choice of values of h and h*. With larger values of the
340 MLD, the relative part of the air-sea flux in the DIC and O₂ measurements would have been
341 smaller and make the slope of the oxygen-carbon relationship closer to 1 as in figure 8.
342 Further, the linear distribution of the data points (figure 9) demonstrates that our technique
343 satisfactorily identifies the biological signature during the selected periods that we have
344 considered.

345 In table 2 (columns 3 and 5), we note the larger contribution of the air-sea exchange for
346 oxygen (positive) relatively to carbon (negative), with a mean ratio of the absolute values
347 close to 6. In the calculation of NCP, the contribution of CO₂ air-sea exchange is low, and
348 varies between 7% and 25% of the measured change of DIC. By contrast, for oxygen, air-sea
349 exchange represents 50% to 135% of the outgassing of O₂ and hence has the ability to have
350 first order control over calculations of NCP. This situation occurs during observations made
351 during the 11-13 December period, when it is not been possible to isolate the oxygen
352 biological signal due to the large air-sea flux.

353

354 This is an issue regarding the in situ estimates of NCP based on dissolved oxygen argon
355 measurements at the ocean surface (Cassar et al, 2009) in high wind regions when the air-sea
356 flux is large. NCP based on O₂ measurements have to be considered with caution as long as
357 the biological contribution is a small term relative to the air-sea exchange one.

358 Simultaneous measurements of oxygen and carbon ratios on oceanographic moorings have
359 been reported in a few situations in tropical or mid latitudes. Lefèvre and Merlivat (2012),
360 based on data in the tropical Atlantic Ocean on a Pirata mooring equipped with a Carioca
361 pCO₂ sensor and an oxygen optode found an O₂/DICratio ranging between -1.0 and -1.3.

362 Johnson [2010], using simultaneous measurements of O₂ and DIC, at two moorings M1 and
363 M2 off Monterey Bay, in California, found -0.77 ± 0.02 and $\pm 0.93 \pm 0.03$ respectively for the
364 O₂: TCO₂ ratio. He explains these low values by the different impact of gas exchange on DIC
365 and O₂, the gas exchange for O₂ being 10 times faster than for CO₂. Martz et al (2014) use
366 autonomous oxygen and dissolved inorganic carbon observations to examine the oxygen
367 carbon relationship at an upwelling site in the Southern California Current System. They
368 compute a mean value of O₂/DIC equal to -1.20 ± 0.01 and conclude that it is in good
369 agreement with Redfield ratio, in spite a number different of the theoretical value of the
370 Redfield ratio, 1.30.

371 We think that the distribution of our observed simultaneous biological changes of DIC and O₂
372 (figure 9) exhibit convincingly a spectrum of values ranging from near 100% new production
373 to 100% regenerated production regime.

374 **4.4 Carbon NCP and dissolved iron**

375 In figure 4, the trajectory of the buoy is superposed on a mapping of the age of the water
376 parcels since they have left the plateau where they are loaded with iron (d'Ovidio et al.,
377 2015). The rate of change of the horizontal dissolved iron supply, DFe, downstream the
378 plateau is modeled with an exponential decay of the initial on-plateau iron stock in the water

379 column.

380 The data in figure 4 can be interpreted as representative of the changes of the stock of DFe in
381 the ocean upper layer (0-150m), the largest DFe concentrations in the youngest waters. It is
382 interesting to emphasize, at least qualitatively, the relationship between the distribution of
383 DFe and the signature of the biology on the DIC and O₂ concentrations measured along the
384 trajectory of the buoy. As a first example, when the buoy escapes the rich DFe waters on 15-
385 16 November (the cyan square in figure 4) large abrupt changes of DIC (an increase) and O₂
386 (a decrease) are observed (figure 7), suggesting the lack of organic matter production in the
387 absence of iron.

388 A decrease of NCP from $\sim 132 \text{mmolm}^{-2} \text{d}^{-1}$ to $\sim 65 \text{mmolm}^{-2} \text{d}^{-1}$ is computed between the 23-28
389 November and 30 November- 13 December periods. During this time interval, the buoy meets
390 water with ages respectively of 35 and 50 days (the cyan dots in figure 4). Following the
391 exponential decay of the stock of DFe as a function of the age of the water parcel, a decrease
392 of DFe concentrations roughly by a factor 2 is calculated (d'Ovidio et al 2015), indicating that
393 the concentration of DFe control the organic carbon production regime. During the KEOPS 2
394 expedition, at station F-L, the age of the water is 20 days (d'Ovidio et al, 2015) and NPP is
395 equal to $315 \text{mmolm}^{-2} \text{d}^{-1}$ (Cavagna et al, 2014). Assuming that the value of NPP depends only
396 on the stock of DFe, NPP in aged waters, respectively 35 and 50 days old, would be
397 respectively equal to $160 \text{mmol m}^{-2} \text{d}^{-1}$ and $82 \text{mmol m}^{-2} \text{d}^{-1}$ assuming a removal constant equal
398 to 0.045d^{-1} . NCP/NPP ratios are then respectively equal to 0.82 and 0.73. These numbers are
399 close to the f ratio, 0.9, measured by (Cavagna et al., 2014, figure 4) at station F-L on the
400 polar front. The choice of MLD equal to 22 and 25 meters in our estimate of NCP instead of
401 20 meters would have met this limit but larger values of MLD are not acceptable.

402 **4.5 Air-sea flux**

403 A striking feature is the abrupt change of the direction of the air-sea CO₂ and O₂ fluxes, from
404 a sink of atmospheric CO₂ at the ocean surface (the opposite for O₂) to a source, on an

405 episodic event on November 16 and on December 16 when the buoy escapes the iron
406 fertilized plume to enter the polar frontal zone (figure 5). It illustrates how the carbon
407 biological pump is at first order controlled by the iron availability in the water in the plume.
408 These observations highlight the necessity to take into consideration the limits of the different
409 water masses in order to spatially extrapolate field measurements of CO₂ air-sea flux in highly
410 dynamic ocean area like the Southern Ocean. This is reinforced in an iron fertilized region, as
411 the distribution of the iron concentration is closely linked to this dynamic environment.

412

413 **5 Summary and Conclusion**

414 Hourly pCO₂ and oxygen measurements have been made along the trajectory of a CARIOCA
415 drifter downstream from the Kerguelen plateau during the austral bloom from 1st November
416 2011 until 12 February 2012. From 1st November to 12 November, the buoy drifted through a
417 cyclonic meander of the polar front, followed it eastward until 16 December, before heading
418 north and entered the polar frontal zone. The surface water is supersaturated in oxygen until
419 16 December while pCO₂ ocean is smaller than pCO₂ atmosphere, suggesting that biological
420 production dominates. North of the polar frontal zone, the ocean is a source of CO₂ for the
421 atmosphere and a sink of oxygen.

422 Using an alkalinity-salinity relationship, DIC is calculated from pCO₂ and alkalinity. Net
423 community production is calculated from changes of DIC and / or oxygen over short periods
424 of time when biological activity is present and no mixing is encountered. NCP values
425 obtained from 23 November to 13 December decrease from 140± 7 mmol C m⁻²d⁻¹ to 60± 12
426 mmol C m⁻²d⁻¹. Concomitant O₂ increases and DIC decreases allow the calculation of the
427 oxygen carbon stoichiometric ratio O₂/C in organic matter (dissolved and particulate) after
428 subtracting the contribution of CO₂ and O₂ air-sea gas exchange. O₂/C values range between
429 1.1 and 1.4 as expected for new and regenerated biological production regimes.

430 In the vicinity of the polar front, within the downstream plateau Kerguelen plume, the
431 absorbed CO₂ air-sea flux is equal to -8mmolm⁻²d⁻¹ and the O₂ outgassing equal to
432 +38mmolm⁻²d⁻¹. In the polar frontal zone from 16 December 2011 to 12 February 2012, the
433 ocean surface is a source of CO₂ for the atmosphere equal to +5mmolm⁻²d⁻¹ and a sink for O₂
434 equal to -48mmolm⁻²d⁻¹. The abrupt simultaneous changes of the sign of the air-sea CO₂ and
435 O₂ fluxes when the buoy crosses the polar front show the dominant contribution westward in
436 the iron fertilized Kerguelen plume of biology, which is characterised by an absorption of
437 CO₂ and an outgassing of O₂. Within the plume, a comparison between the biological DIC
438 uptakes localized on a mapping of the modeled stock of dissolved iron, DFe, in the water
439 column shows a coupling between the amount of DFe and the carbon net community
440 production. This highlights that the phytoplankton growth rates appear to increase directly
441 with the level of iron availability. However a patchy distribution of iron within the plume can
442 lead to a patchy organic carbon production and consequently affect unevenly in time and
443 space the uptake of atmospheric CO₂. For instance, this is well illustrated when the buoy
444 crosses the polar front on 16 December. This study points that care should be taken when
445 extrapolating sparse air-sea flux measurements observations without an understanding of the
446 hydrodynamic features of the upper ocean.

447

448 **Acknowledgments**

449 We are grateful to N. Martin from LOCEAN for software development and to L. Beaumont
450 from DT-INSU, who supervised the CARIOCA preparation. We thank S. Blain, project
451 leader, and B. Quéguiner, chief scientist, as well as the captain and crew of R.R.V. Marion
452 Dufresne and the staff at the French Polar Institute (IPEV) who provided logistic support.
453 Special thanks to Claire Lo Monaco for access to pCO₂ results and Dominique Lefèvre for

454 access to O₂ results. We thank Y. Park for having provided the data files for correctly
455 positioning the polar front. We also enjoyed the stimulating discussions with N. Cassar during
456 his stay at LOCEAN and the comments of S. Blain in the course of the preparation of the
457 manuscript.

458 The research leading to these results was supported through EU FP6 project CARBOOCEAN
459 (contract 511176) and EU FP7 project CARBOCHANGE “Changes in carbon uptake and
460 emissions by oceans in a changing climate” which received funding from the European
461 Commission’s Seventh Framework Program under grant agreement no. 264879. The KEOPS2
462 project was funded by the French institutes INSU (Institut National des Sciences de
463 l’Univers), IPEV (Institut Paul Emile Victor) and ANR (Agence Nationale de la Recherche).

464

465 **References**

466 Blain, S., Quéguiner, B., Armand, L., Belviso, S., Bombled, B., Bopp, L., Bowie, A., Brunet,
467 C., Brussaard, C., Carlotti, F., Christaki, U., Corbière, A., Durand, I., Ebersbach, F.,
468 Fuda, J.-L., Garcia, N., Gerringa, L., Griffiths, B., Guigue, C., Guillerm, C., Jacquet,
469 S., Jeandel, C., Laan, P., Lefèvre, D., Lo Monaco, C., Malits, A., Mosseri, J.,
470 Obernosterer, I., Park, Y.-H., Picheral, M., Pondaven, P., Remenyi, T., Sandroni, V.,
471 Sarthou, G., Savoye, N., Scouarnec, L., Souhaut, M., Thuiller, D., Timmermans, K.,
472 Trull, T., Uitz, J., van Beek, P., Veldhuis, M., Vincent, D., Viollier, E., Vong, L. and
473 Wagener, T. (2007) Effect of natural iron fertilization on carbon sequestration in the
474 Southern Ocean, *Nature*, 446, 1070-1074, doi:10.1038/nature05700.

475 Blain, S., Sarthou, G., Laan, P., 2008. Distribution of dissolved iron during the natural iron
476 fertilization experiment KEOPS (Kerguelen Plateau, Southern Ocean), *Deep Sea
477 Research Part II: Topical Studies in Oceanography* 55, 594-605.

478 Borrione, I., and Schlitzer, R. (2013). Distribution and recurrence of phytoplankton blooms
479 around South Georgia, Southern Ocean, *Biogeosciences*, 10, 217-231.

480 Boutin J., Merlivat L., Hénocq C., Martin N., and J.B. Sallée (2008) Air-sea CO₂ flux
481 variability in frontal regions of the Southern Ocean from CARIOCA drifters,
482 *Limnol. Oceanogr.* 53: 2062-2079

483 Boutin, J., and Merlivat, L. (2009). New in situ estimates of carbon biological production
484 rates in the Southern Ocean from CARIOCA drifter measurements, *Geophys. Res.*
485 *Lett.*, **36**, L13608.

486 Boyd, P.W., Jickells, T., Law, C.S., Blain, S., Boyle, E.A., Buesseler, K.O., Coale, K.H.,
487 Cullen, J.J., de Baar, H.J.W., Follows, M., Harvey, M., Lancelot, C., Levasseur, M.,
488 Owens, N.P.J., Pollard, R., Rivkin, R.B., Sarmiento, J., Schoemann, V., Smetacek, V.,
489 Takeda, S., Tsuda, A., Turner, S., Watson, A.J., 2007. Mesoscale iron enrichment
490 experiments 1993-2005: Synthesis and future directions. *Science* 315, 612-617.

491 Cassar, N., Barnett, B.A., Bender, M.L., et al, (2009), Continuous high frequency dissolved
492 O₂/Ar measurements by equilibrator inlet mass spectrometry, *Analytical Chemistry*,
493 81, 5, 1855-1864.

494 Cavagna, A.J., Fripiat, F., Elskens, M., Dehairs, F., Mangion, P., Chirurgien, L., Closset, I.,
495 Lasbleiz, M., Flores-Leiva, L., Cardinal, D., Leblanc, K., Fernandez, C., Lefèvre, D.,
496 Oriol, L., and B. Quéguiner, (2014), Biological productivity regime and associated N
497 cycling in the surface waters over and downstream the Kerguelen Island area,
498 Southern Ocean, *Biogeosciences Discuss.*, 11, 18073–18104, doi:10.5194/bgd-11-
499 18073-2014

500 Copin-Montegut, C. (2000), Consumption and production on scales of a few days of inorganic
501 carbon, nitrate and oxygen by the planktonic community: results of continuous

502 measurements at the Dyfamed Station in the northwestern Mediterranean Sea (May
503 1995), *Deep-Sea Research I*, 47, 447-477.

504 Dickson, A.G., and Millero, F.J. (1987), A comparison of the equilibrium constants for the
505 dissociation of carbonic acid in seawater media. *Deep-Sea Res.*, **34**, 1733-1743.

506 d'Ovidio, F., et al. (2015), The biogeochemical structuring role of horizontal stirring:
507 Lagrangian perspectives on iron delivery downstream of the Kerguelen plateau,
508 *Biogeosciences Discuss.*, 12, 779–814, doi:10.5194/bgd-12-779-2015

509 Friedlingstein, P., et al. (2006), Climate-carbon cycle feedback analysis: Results from the
510 (CMIP)-M-4 model intercomparison, *Journal of Climate*, 19(14), 3337-3353.

511 Garcia, H.E., and Gordon, L.I. (1992), Oxygen solubility in seawater: better fitting equations.
512 *Limnol. Oceanogr.*, **37** (6), 1307-1312.

513 Gruber, N., et al. (2009), Oceanic sources, sinks, and transport of atmospheric CO₂, *Global*
514 *Biogeochem. Cycles*, 23. GB1005, doi:10. 1029/2008GB003349.

515 Johnson, K. S. (2010), Simultaneous measurements of nitrate, oxygen, and carbon dioxide on
516 oceanographic moorings: Observing the Redfield ratio in real time, *Limnol.*
517 *Oceanogr.*, 55(2), 615–627, doi:10.4319/lo.2009.55.2.0615.

518 Jouandet et al. (2008), A seasonal carbon budget for a naturally iron-fertilized bloom over the
519 Kerguelen Plateau in the Southern Ocean, *Deep-Sea Research II*, 55, 856–867.

520 Laws, E. A. (1991), Photosynthetic quotients, new production and net community production
521 in the open ocean, *Deep Sea Research*, 38, 143–167, doi:10.1016/0198-
522 0149(91)90059-O.

523 Lefevre, D., Guigue, C., Obernosterer, I., (2008). The metabolic balance at two contrasting
524 sites in the Southern Ocean: The iron-fertilized Kerguelen area and HNLC waters.

525 *Deep-Sea Research II*, 55, 766–776

526 Lefèvre, N., and L. Merlivat (2012), Carbon and oxygen net community production in the
527 eastern tropical Atlantic estimated from a moored buoy, *Global Biogeochem. Cycles*,
528 26, GB 1009, doi: 10.1029/2010 GB004018.

529 Lenton A., B. Tilbrook, R. M. Law, D. Bakker, S. C. Doney, N. Gruber, M. Ishii, M.
530 Hoppema, N. S. Lovenduski, R. J. Matear, B. I. McNeil, N. Metzl, S. E. Mikaloff
531 Fletcher, P. M. S. Monteiro, C. Rödenbeck, C. Sweeney, and T. Takahashi. (2013),
532 Sea-air CO₂ fluxes in the Southern Ocean for the period 1990–2009, *Biogeosciences*,
533 10, 4037-4054, doi: 10.5194/bg-10-4037-2013 .

534 Le Quere, C., T. Takahashi, E. T. Buitenhuis, C. Rodenbeck, and S. C. Sutherland (2010),
535 Impact of climate change on the global oceanic sink of CO₂, *Global Biogeochem.*
536 *Cycles*, doi: 10.1029/2009GB003599.

537 Lo Monaco, C., Metzl, N., d’Ovidio, F., Llort, J., and C. Ridame (2014), Rapid establishment
538 of the CO₂ sink associated with Kerguelen’s bloom observed during the
539 KEOPS2/OISO20 cruise, *Biogeosciences Discuss.*, 11, 17543–17578,
540 doi:10.5194/bgd-11-17543-2014

541 Martz, T., U. Send, M. D. Ohman, Y. Takeshita, P. Bresnahan, H.-J. Kim, and S.H. Nam
542 (2014), Dynamic variability of biogeochemical ratios in the Southern California
543 Current System, *Geophys. Res. Lett.*, 41, 2496–2501, doi:10.1002/ 2014GL059332.

544 Mehrbach, C., Culberson, C.H., Hawley, J.E., and Pytkowicz, R.M. (1973), Measurement of
545 the apparent dissociation constants of carbonic acid in seawater at atmospheric
546 pressure. *Limnol. Oceanogr.*, **18**, 897-907.

547 Merlivat, L., M. Gonzales-Davila, G. Caniaux, J. Boutin, and G. Reverdin, (2009), Mesoscale
548 and diel to monthly variability of CO₂ and carbon fluxes at the ocean surface in the

549 northeastern Atlantic, *J. Geophys. Res.*, 114, C03010, doi:10.1029/2007JC004657.

550 Merlivat, L., Boutin, J., Antoine, D., (2014) Roles of biological and physical processes in
551 driving seasonal air-sea CO₂ flux in the Southern Ocean: New insights from
552 CARIOCA pCO₂, *J. Mar. Syst.*, <http://dx.doi.org/10.1016/j.jmarsys.2014.04.015>

553 Metzl, N., B. Tilbrook, and A. Poisson (1999), The annual fCO₂ cycle and the air-sea CO₂
554 flux in the sub-Antarctic Ocean, *Tellus Series B-Chemical and Physical*
555 *Meteorology*, 51(4), 849-861

556 Park, Y.-H., F. Vivier, F. Roquet, and E. Kestenare (2009), Direct observations of the ACC
557 transport across the Kerguelen Plateau, *Geophys. Res. Lett.*, 36, L18603,
558 doi: 10.1029/2009GL039617.

559 Park, Y.-H., and F. Vivier (2011), Circulation and hydrography over the Kerguelen Plateau, in
560 *The Kerguelen Plateau: marine ecosystem and fisheries*, edited by G. Duhamel et al.,
561 pp.597 43-55, Cybium, Paris.

562 Park, Y.-H., I. Durand, E. Kestenare, G. Rougier, M. Zhou, F. d'Ovidio, C. Cotté, J.-H. Lee
563 (2014), Polar Front around the Kerguelen Islands: An up-to-date determination and
564 associated circulation of surface/subsurface waters, *J. Geophys. Res.*, doi: 10.
565 1002/2014JC010061.

566 Pollard, R.T., Salter, I., Sanders, R.J., Lucas, M.I., Moore, C.M., Mills, R.A., Statham, P.J.,
567 Allen, J.T., Baker, A.R., Bakker, D.C.E., Charette, M.A., Fielding, S., Fones, G.R.,
568 French, M., Hickman, A.E., Holland, R.J., Hughes, J.A., Jickells, T.D., Lampitt, R.S.,
569 Morris, P.J., Nedelec, F.H., Nielsdottir, M., Planquette, H., Popova, E.E., Poulton,
570 A.J., Read, J.F., Seeyave, S., Smith, T., Stinchcombe, M., Taylor, S., Thomalla, S.,
571 Venables, H.J., Williamson, R., Zubkov, M.V., 2009. Southern Ocean deep-water
572 carbon export enhanced by natural iron fertilization, *Nature* 457, 577-580.

573 Stanley, R. H. R., W. J. Jenkins, D. E. Lott III, and S. C. Doney (2009), Noble gas constraints
574 on air-sea gas exchange and bubble fluxes, *J. Geophys. Res.*, 114, C11020, doi:
575 10.1029/2009JC005396

576 Sweeney, C., Gloor, E., Jacobson, A.R., Key, R.M., McKinley, G., Sarmiento, J.L., and
577 Wanninkhof, R. (2007), Constraining global air-sea gas exchange for CO₂ with recent
578 bomb ¹⁴C measurements. *Global Biogeochem. Cycles*, **21**, doi:
579 10.1029/2006GB002784.

580 Takahashi, T., et al. (2009), Climatological mean and decadal change in surface ocean
581 pCO₂, and net sea-air CO₂ flux over the global oceans, *Deep-Sea Research Part II-*
582 *Topical Studies in Oceanography*, 56(8-10), 554-577.

583 Taylor, J.R and Ferrari, R. (2011), Ocean fronts trigger high latitude phytoplankton blooms.
584 *Geophys. Res. Lett.*, 38, L23601, doi:10.1029/2011GL049312.

585 Trull, T.W., Davies, D. M., Dehairs, F., Cavagna, A.J., Lasbleiz, M., Laurenceau, E.C.,
586 d'Ovidio, F., Planchon, F., Leblanc, K., Quéguiner, B., and S. Blain, (2015),
587 Chemometric perspectives on plankton community responses to natural iron
588 fertilization over and downstream of the Kerguelen plateau in the Southern Ocean,
589 *Biogeosciences* 12, 1029-1056, doi:10.5194/bg-12-1029-2015

590 Wanninkhof, R.H. (1992), Relationship between wind speed and gas exchange over the
591 ocean. *J. Geophys. Res.*, **97 (C5)**, 7373-7382.

592 Weiss, R.F. (1974), CO₂ in water and seawater: the solubility of a non-ideal gas. *Mar. Chem.*,
593 **2**, 203-215.

594 Woolf, D.K., and Thorpe, S.A. (1991), Bubbles and the air-sea exchange of gases in near-
595 saturation conditions. *J. Mar. Res.*, **49**, 435-466.

596

597 Table 1. Difference between the extrema of DIC and O₂ measured in the warm surface layer598 (columns 4 and 6). In bold, mean values of DIC and O₂ changes over consecutive mornings599 (columns 5 and 7), CO₂ and O₂ air-sea flux (columns 8 and 9).

600

Date	Latitude	SST	DIC _{min} -DIC _{max}	dDIC _{max} /dt	O _{2max} -O _{2min}	dO _{2min} /dt	F _{CO2}	F _{O2}
	Longitude	°C	μmol kg ⁻¹	μmol kg ⁻¹	μmol kg ⁻¹	μmol kg ⁻¹	mmol m ⁻² d ⁻¹	mmolm ⁻² d ⁻¹
1	2	3	4	5	6	7	8	9
18 Nov	49.3°S76.4°E	4.2	-6.46±1.00		7.19±1.00			
23-25 Nov	50.1°S77°4E	4.3		-4.72±0.23		3.74±0.54	-8.21	42.9
23 Nov			-11.50±1.00		9.77±1.00			
24 Nov			-10.09±1.00		11.41±1.00			
26-28 Nov	50.4°S77.3°E	4.4		-4.22±0.85		3.90±1.01	-5.83	38.5
27 Nov			-9.35±1.00		8.39±1.00			
30Nov4Dec	50.4°S79.8°E	4.5		-1.76±0.43		1.71±0.32	-9.13	47.4
30 Nov			-8.50±1.00		6.17±1.00			
1 Dec			-5.79±1.00		5.73±1.00			
2 Dec			-7.80±1.00		7.25±1.00			
11-13 Dec	50.2°S81.4°E	4.6		-2.10±0.65			-10.49	61.0

601

602

603

603
 604 Table 2. Biological changes (columns 2 and 4) and air-sea flux changes (columns 3 and 5) of
 605 DIC and O₂. In bold, mean values over consecutive mornings. Calculated values of NCP
 606 carbon and NCP oxygen (columns 6 and 7)

607

Date	dDIC _{bio} μmol kg ⁻¹	dDIC _{air-sea} μmol kg ⁻¹	dO ₂ _{bio} μmol kg ⁻¹	dO ₂ _{air-sea} μmol kg ⁻¹	NCP _C mmol C m ⁻² d ⁻¹	NCP _{O₂} mmol O ₂ m ⁻² d ⁻¹
1	2	3	4	5	6	7
18 Nov	-6.79±1.00	-0.32±0.10	10.23±1.35	3.03±0.91		
23-25 Nov	-5.12±0.26	-0.40±0.12	5.83±0.83	2.09±0.63	-140±7	160±23
23 Nov	-12.43±1.04	-0.93±0.28	14.18±1.66	4.41±1.32		
24 Nov	-10.47±1.00	-0.38±0.11	13.88±1.24	2.47±0.74		
26-28 Nov	-4.50±0.85	-0.28±0.09	5.78±1.16	1.87±0.56	-124±23	159±31
27 Nov	-9.74±1.01	-0.39±0.12	10.85±1.24	2.46±0.74		
30Nov4Dec	-2.20±0.45	-0.44±0.13	4.02±0.76	2.31±0.69	-60±12	111±20
30 Nov	-9.07±1.01	-0.58±0.17	8.78±1.27	2.60±0.78		
1 Dec	-6.44±1.02	-0.66±0.20	9.78±1.57	4.05±1.22		
2 Dec	-8.38±1.02	-0.58±0.17	10.88±1.48	3.63±1.09		
11-13 Dec	-2.61±0.67	-0.51±0.15		2.96±0.89	-72±17	

608

FIGURE CAPTIONS

610 **Figure 1.** Trajectory followed by the Carioca drifter from 1 November 2011 to 12 February
611 2012 (red line). The green dots and letters indicate the location and time where the data
612 indicate a large signature of biological effects. The grey diamonds indicate high isolated
613 salinity anomalies. The buoy enters the polar frontal zone at the location of the blue arrow.
614 The pink dotted line represents the location of the subantarctic front, SAF, the blue dashed
615 line shows the location of the polar front (Park et al, 2009, 2011) and the black line, the
616 location of the polar front based on KEOPS 2 observations, PF_Park, (Park et al,2014). The
617 black dots indicate the location of the KEOPS 2 stations,TEW-7,TEW-8,NPF-L, close to the
618 PF.

619 **Figure 2.** Diurnal cycles of SST, DIC and O₂ from 30 November to 4 December 2011. **a** SST
620 (°C) (black, left vertical axis) and DIC ($\mu\text{mol kg}^{-1}$) (grey, right vertical axis).The vertical
621 dashed lines indicate the time of sunrise (blue) and sunset (orange). **b** O₂ ($\mu\text{mol kg}^{-1}$) (black,
622 left vertical axis) and DIC (grey, right vertical axis).

623 **Figure 3.** Spatial extent of phytoplankton blooms over and downstream from the Kerguelen
624 plateau as revealed by satellite ocean color on 6 selected days, from 11 November to 28
625 December 2011. The trajectory followed by the CARIOCA drifter is superposed on the
626 chlorophyll patches (black line). The circles indicate the location of the buoy the same days.

627 **Figure 4.** Lagrangian perspectives on large scale natural iron fertilization on the Kerguelen
628 plateau and in the downstream plume: a snapshot on 25 November 2011.The color code
629 indicates the time in days since leaving the plateau for each water parcel (d'Ovidio et al,
630 2015). The white line indicates the trajectory of the Carioca drifter from 1 November to 31
631 December 2011.The cyan dots indicate the locations where carbon NCP estimates are
632 calculated. The cyan square is the position of the buoy on 16 November (see text).

633 **Figure 5.** Buoy data from 1 November 2011 to 12 February 2012. **a** temperature in °C (black,
634 left vertical axis) and salinity (grey, right vertical axis). **b** T-S diagram: 1 to 11 November,
635 black diamonds- 12 November to 16 December, grey diamonds- 17 December to 12 February,
636 black squares. **c** pCO₂ measured at a depth of 2 meters in μatm (black) and in the atmosphere
637 in μatm (grey). **d** Dissolved oxygen concentration measured at a depth of 2 meters in μmol
638 kg⁻¹(black, left vertical axis) and oxygen saturation in % (grey, right vertical axis). In figure
639 5a, the cyan dashed lines indicate the 12 November and 16 December days (see text). In
640 figure 5b,the red dots indicate the data measured at the KEOPS 2 stations, TEW7, TEW8, F-
641 L.

642 **Figure 6.** Air-sea flux from 1 November 2011 to 12 February 2012 in mmol m⁻²d⁻¹ (positive
643 for outgassing). **a** O₂). **b** CO₂

644 **Figure 7.** Distribution of O₂ in μmol kg⁻¹ (black, left vertical axis) and DIC in μmol kg⁻¹
645 (grey, right vertical axis) between 1 November 2011 and 12 February 2012. The purple dots
646 and lines indicate the periods when NCP estimates have been made. The cyan dashed lines
647 indicates the 12 November and 16 December days and the cyan arrow the 16 November (see
648 text).

649 **Figure 8.** Measured changes (absolute values) of O₂ (μmol kg⁻¹) as a function of measured
650 changes (absolute values) of DIC (μmol kg⁻¹) between consecutive mornings, (dark blue
651 dots), or during the daylight period (light blue dots). The slope of the black dotted line is 1.

652 **Figure 9.** Changes (absolute values) of O₂ (μmol kg⁻¹) attributed to biological activity as a
653 function of changes (absolute values) of DIC (μmol kg⁻¹) attributed to biological activity
654 between consecutive mornings (red dots), or during the daylight period (blue dots). The two
655 dotted lines with a slope of 1.4 and 1.1 respectively characterize the new and regenerated
656 production regime

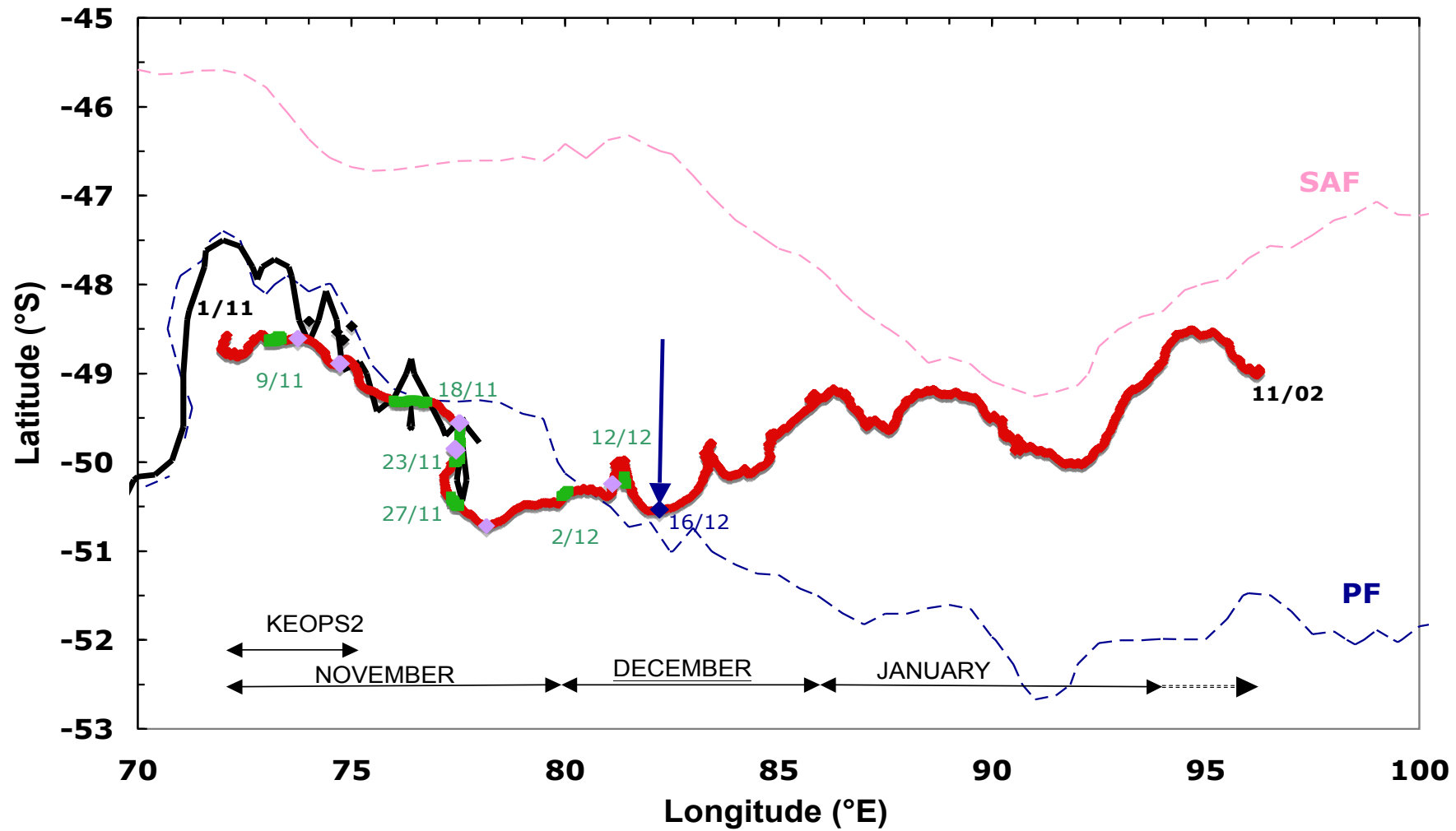
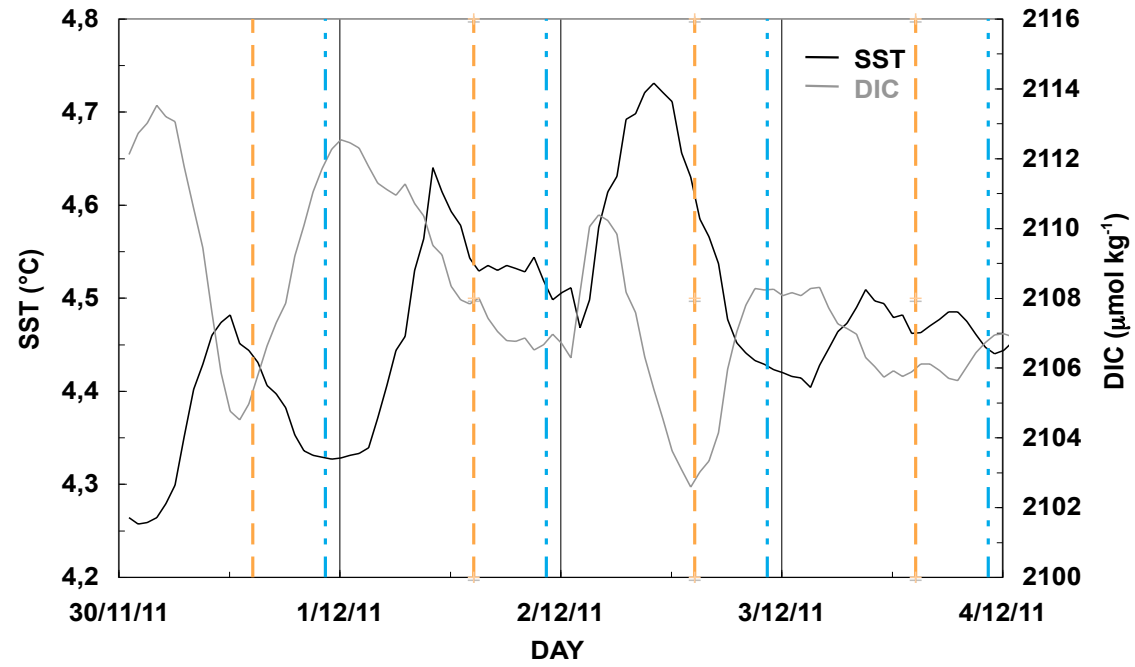
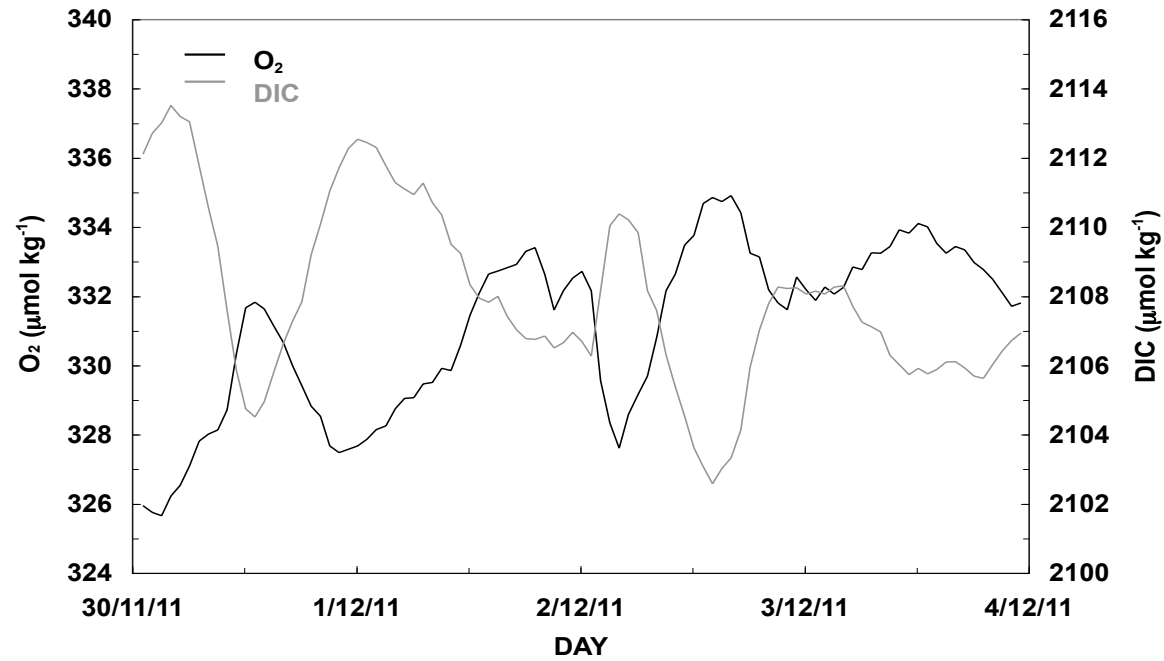


Figure 1

a**b****Figure 2**

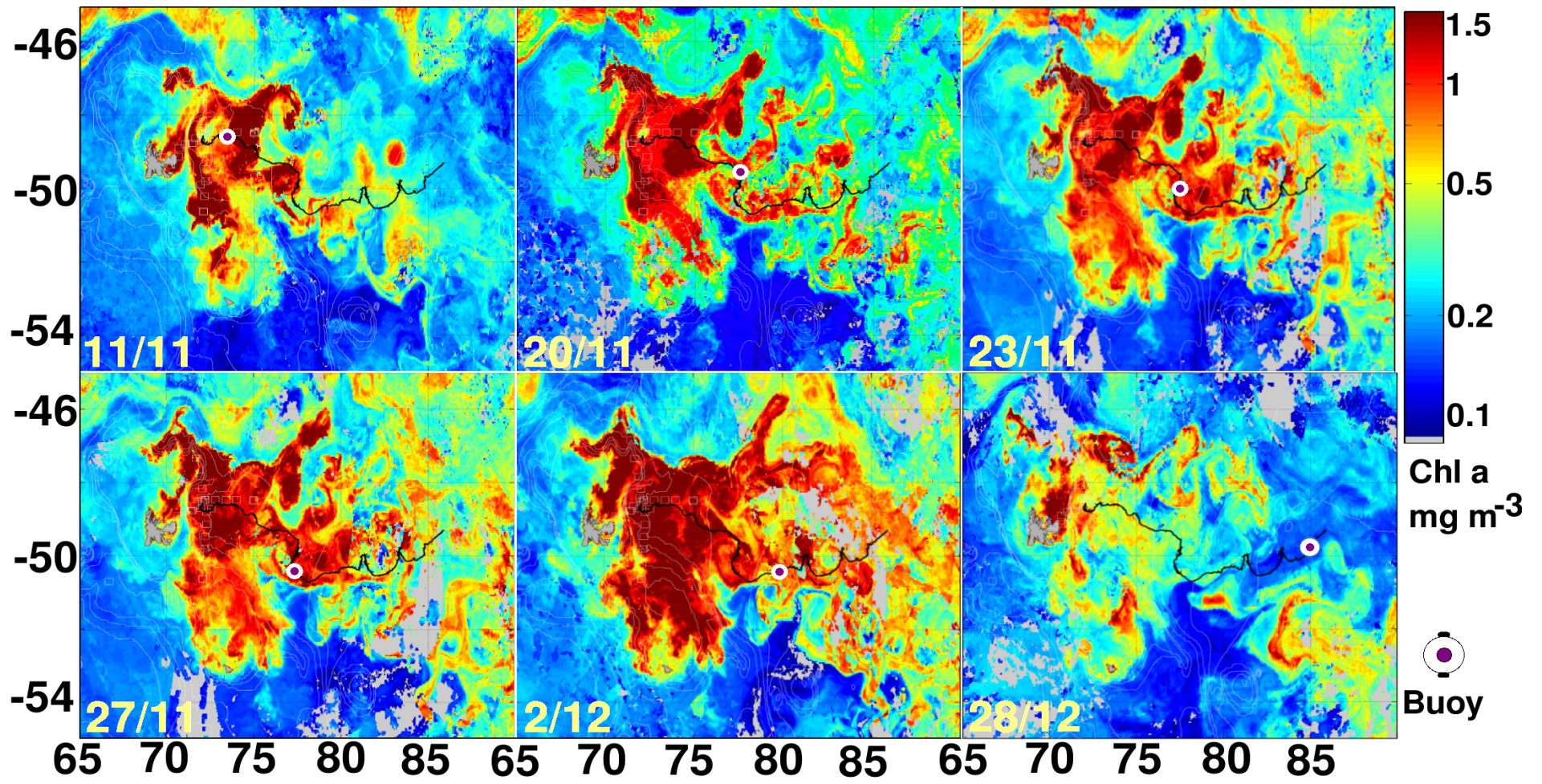


Figure 3

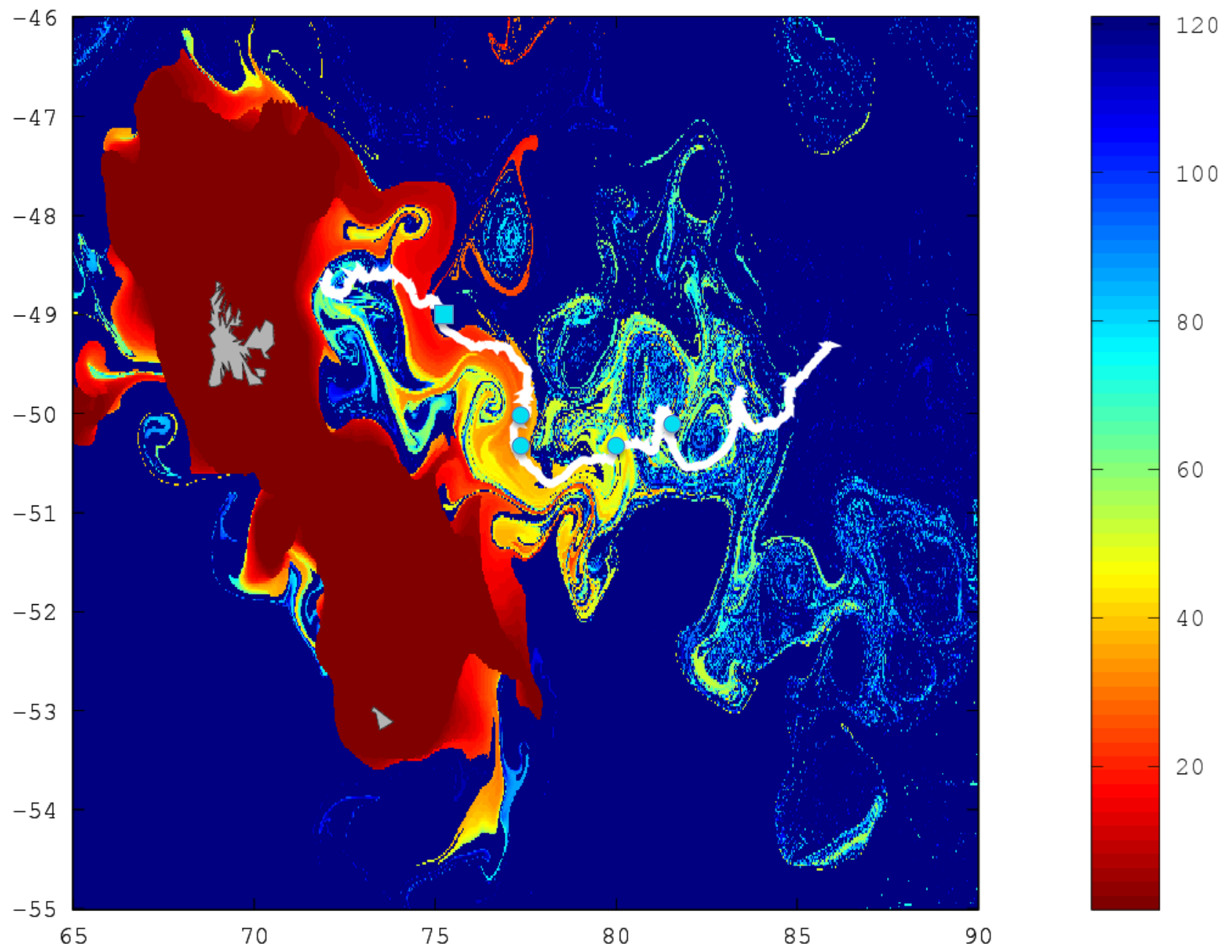


Figure 4

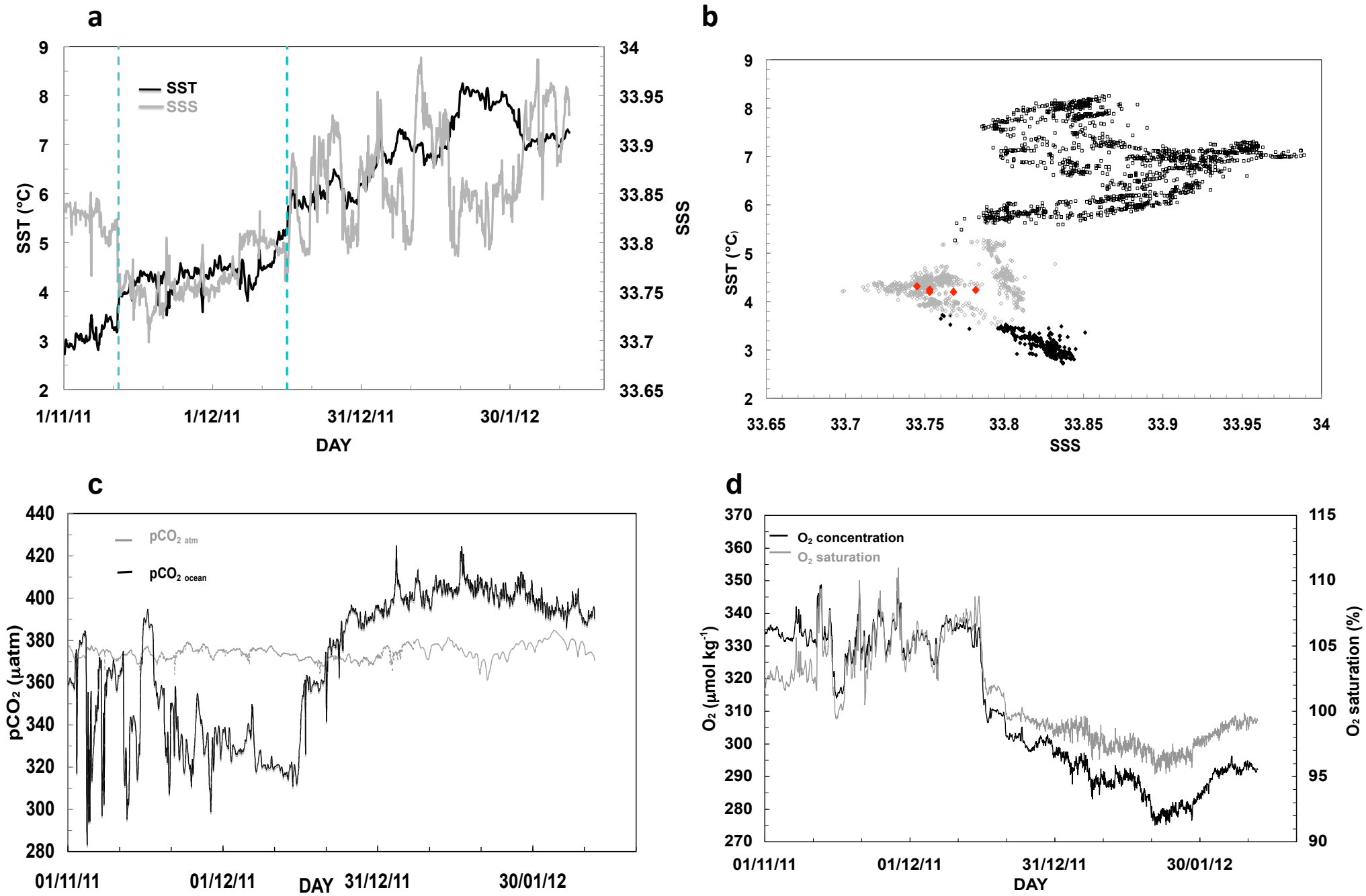


Figure 5

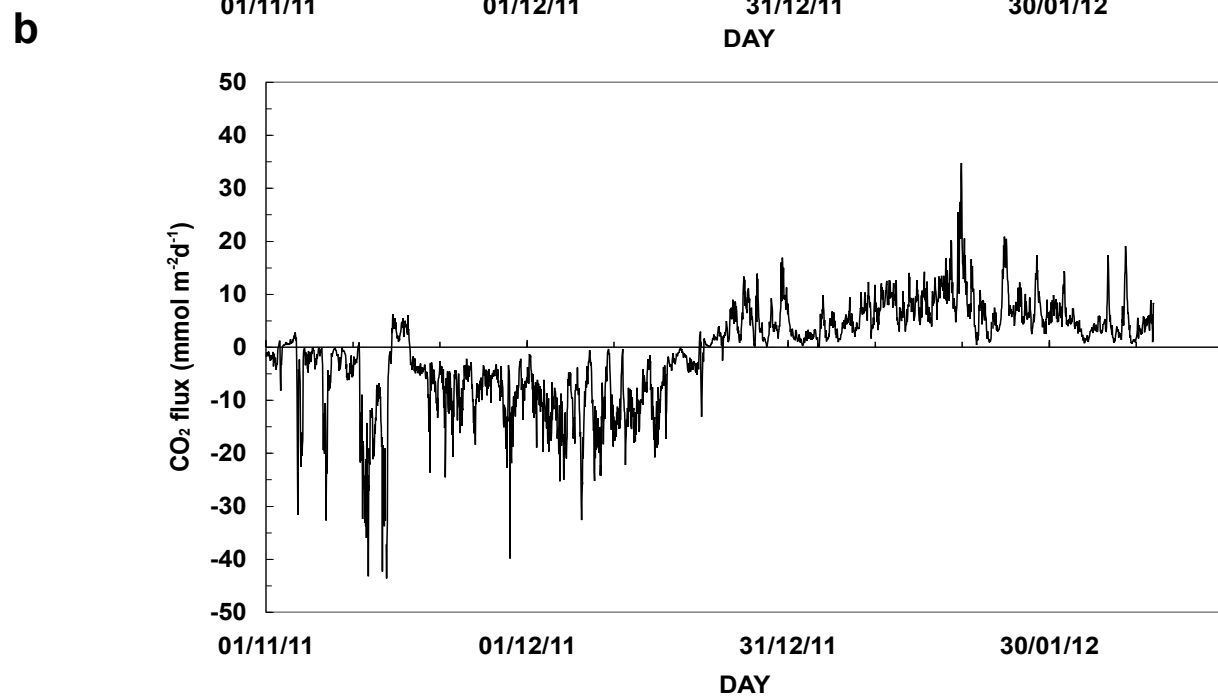
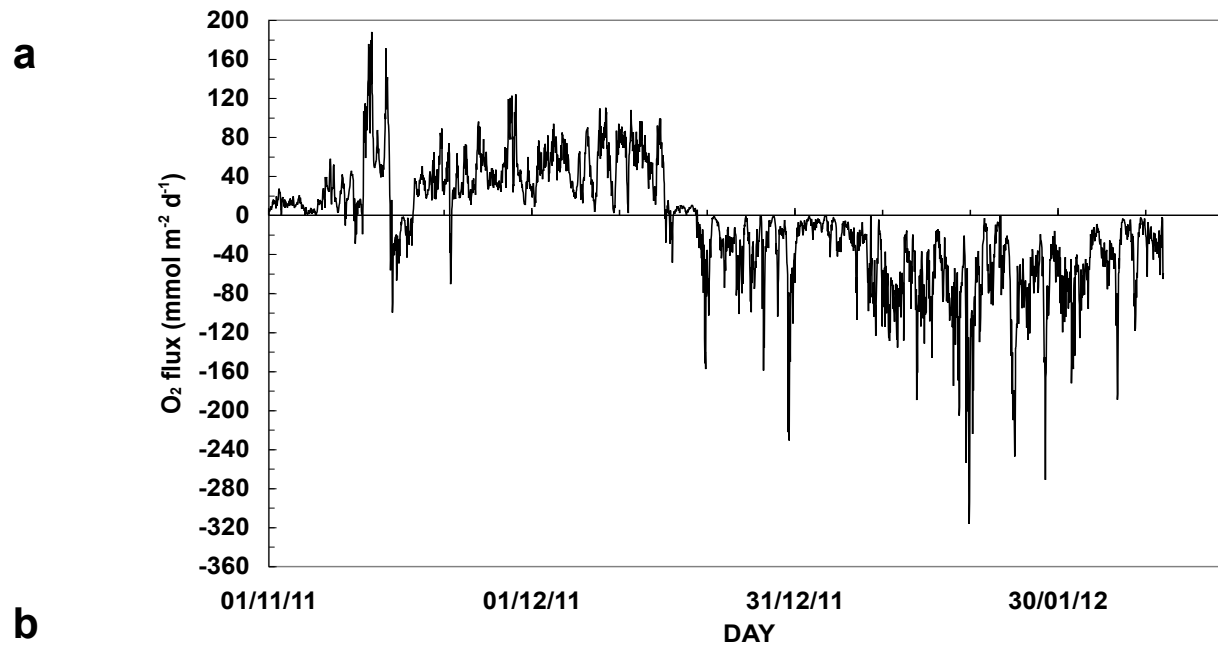


Figure 6

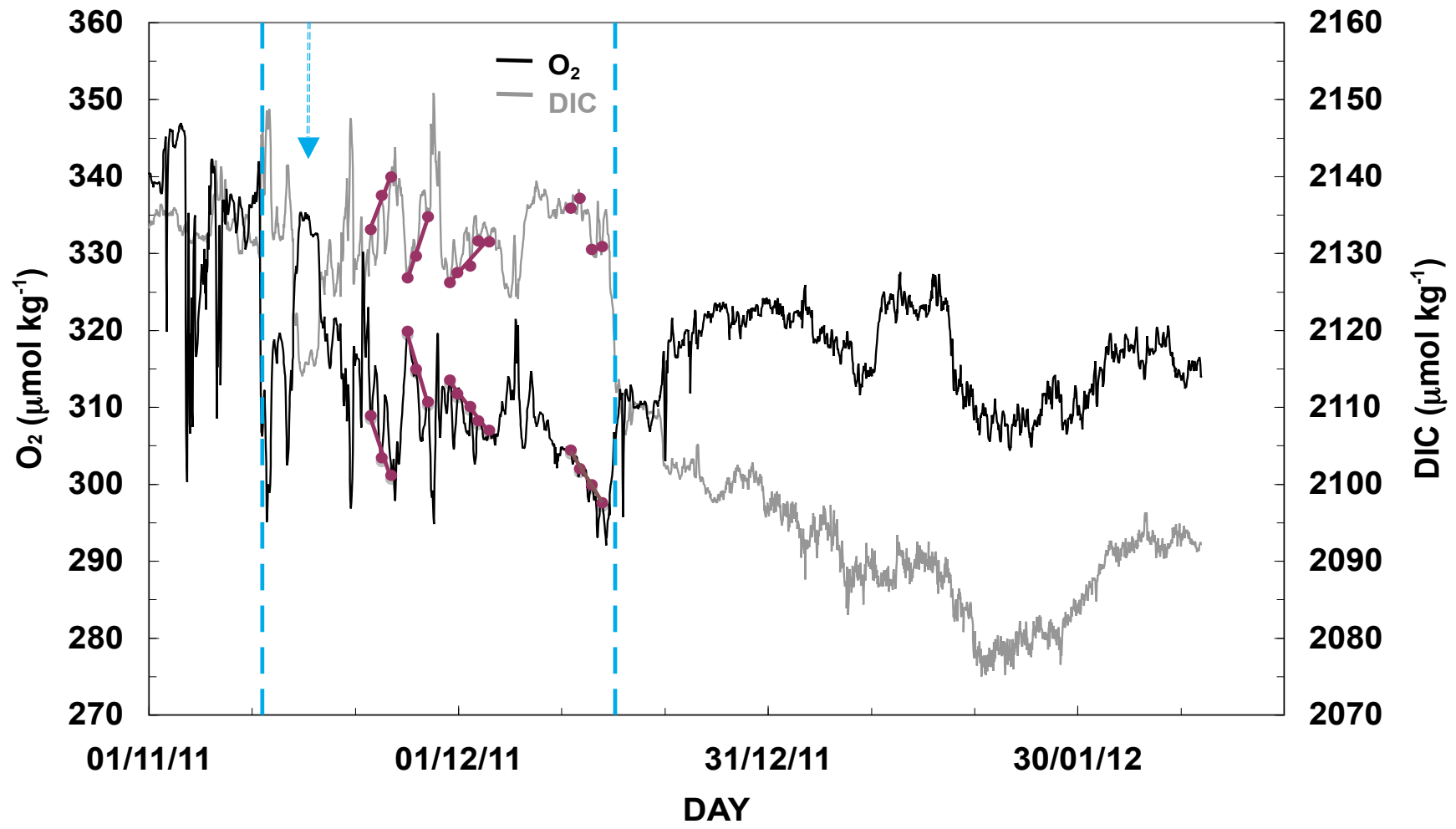


Figure 7

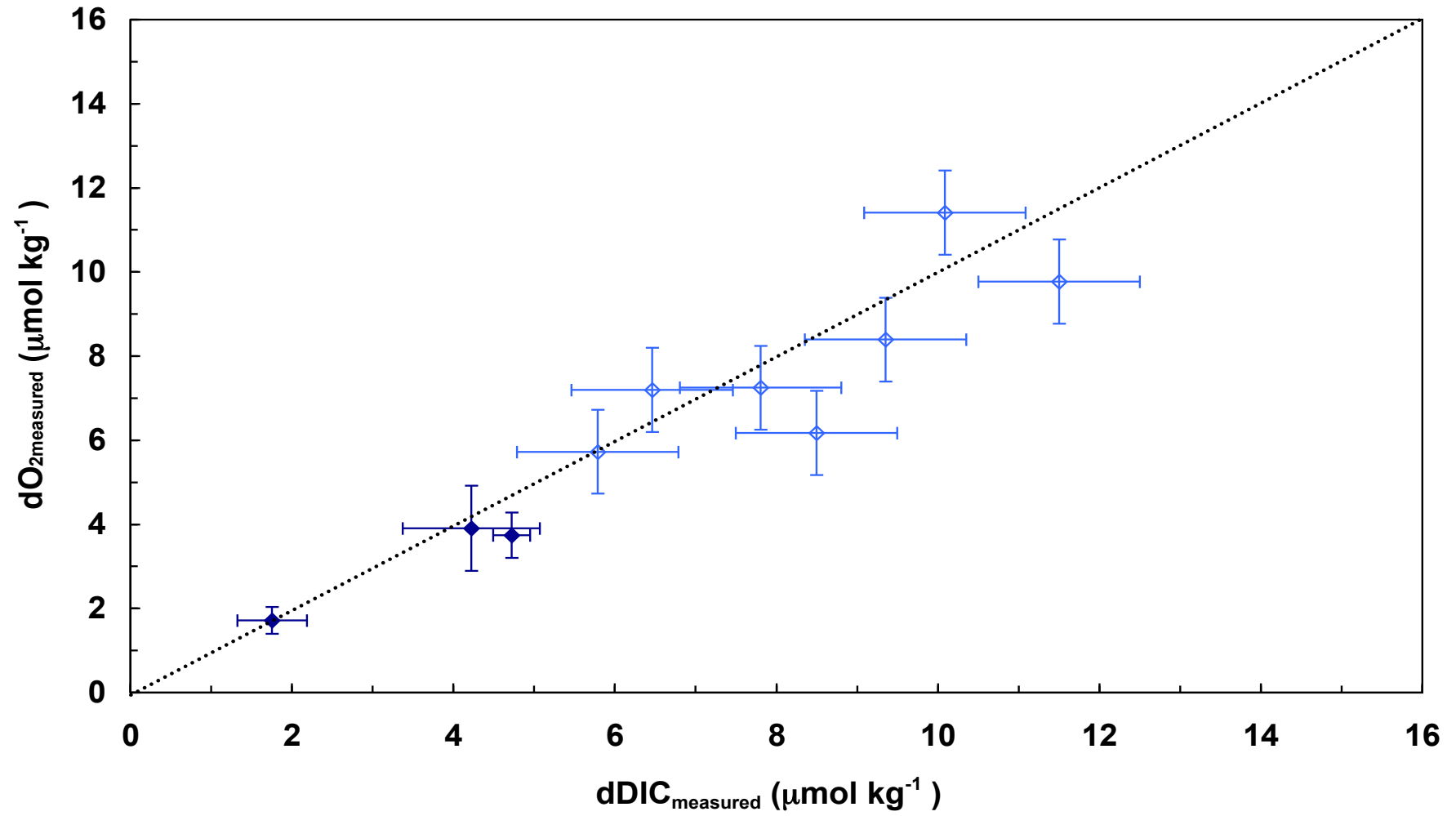


Figure 8

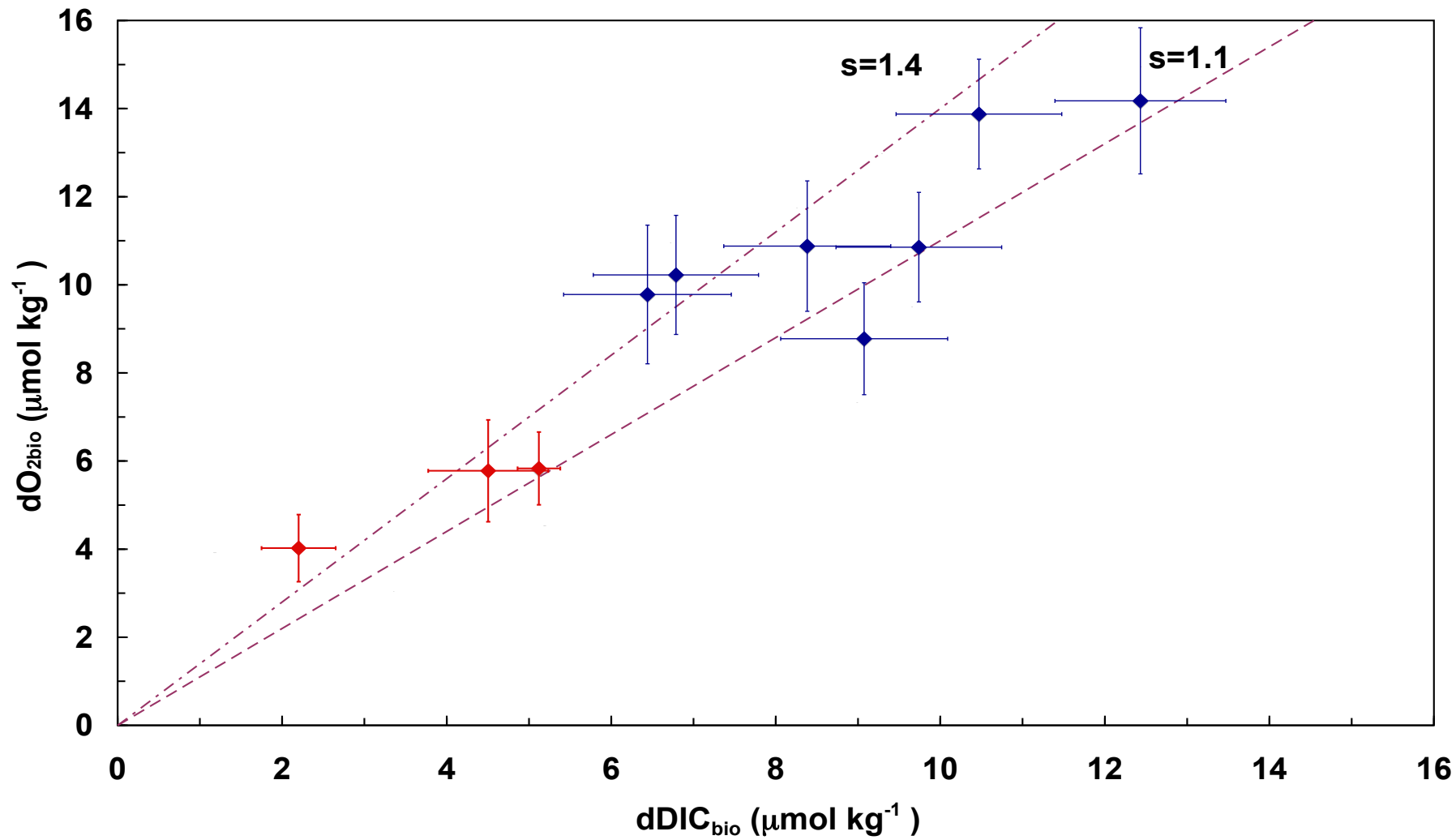


Figure 9